

Global all-sky shortwave direct radiative forcing of anthropogenic aerosols from combined satellite observations and GOCART simulations

Wenying Su,¹ Norman G. Loeb,¹ Gregory L. Schuster,¹ Mian Chin,² and Fred G. Rose³

Received 15 June 2012; revised 16 November 2012; accepted 19 November 2012; published 17 January 2013.

[1] Estimation of aerosol direct radiative forcing (DRF) from satellite measurements is challenging because current satellite sensors do not have the capability of discriminating between anthropogenic and natural aerosols. We combine 3-hourly cloud properties from satellite retrievals with two aerosol data sets to calculate the all-sky aerosol direct radiative effect (DRE), which is the mean radiative perturbation due to the presence of both natural and anthropogenic aerosols. The first aerosol data set is based upon Moderate Resolution Imaging Spectroradiometer (MODIS) and Model for Atmospheric Transport and Chemistry (MATCH) assimilation model and is largely constrained by MODIS aerosol optical depth, but it does not distinguish between anthropogenic and natural aerosols. The other aerosol data set is based upon the Goddard Chemistry Aerosol Radiation and Transport (GOCART) model, which does not assimilate aerosol observations but predicts the anthropogenic and natural components of aerosols. Thus, we can calculate the aerosol DRF using GOCART classifications of anthropogenic and natural aerosols and the ratio of DRF to DRE. We then apply this ratio to DRE calculated using MODIS/MATCH aerosols to partition it into DRF (MODIS/MATCH DRF) by assuming that the anthropogenic fractions from GOCART are representative. The global (60°N–60°S) mean all-sky MODIS/MATCH DRF is -0.51 Wm^{-2} at the top of the atmosphere (TOA), 2.51 Wm^{-2} within the atmosphere, and -3.02 Wm^{-2} at the surface. The GOCART all-sky DRF is -0.17 Wm^{-2} at the TOA, 2.02 Wm^{-2} within the atmosphere, and -2.19 Wm^{-2} at the surface. The differences between MODIS/MATCH DRF and GOCART DRF are solely due to the differences in aerosol properties, since both computations use the same cloud properties and surface albedo and the same proportion of anthropogenic contributions to aerosol DRE. Aerosol optical depths simulated by the GOCART model are smaller than those in MODIS/MATCH, and aerosols in the GOCART model are more absorbing than those in MODIS/MATCH. Large difference in all-sky TOA DRF from these two aerosol data sets highlights the complexity in determining the all-sky DRF, since the presence of clouds amplifies the sensitivities of DRF to aerosol single-scattering albedo and aerosol vertical distribution.

Citation: Su, W., N. G. Loeb, G. L. Schuster, M. Chin, and F. G. Rose (2013), Global all-sky shortwave direct radiative forcing of anthropogenic aerosols from combined satellite observations and GOCART simulations, *J. Geophys. Res. Atmos.*, 118, 655–669, doi:10.1029/2012JD018294.

1. Introduction

[2] The solar direct radiative effect (DRE) is the mean radiative flux perturbation due to the presence of aerosols (both natural and anthropogenic), while the aerosol direct radiative forcing (DRF) is the anthropogenic component of DRE.

Considerable effort has been dedicated to estimating DRE under clear-sky conditions from satellite measurements; global mean clear-sky DRE at the top of the atmosphere (TOA) from various studies agree reasonably well. Over ocean, the TOA DRE is $-5.5 \pm 0.7 \text{ Wm}^{-2}$ (mean \pm standard deviation), and over land the TOA DRE is $-4.9 \pm 0.45 \text{ Wm}^{-2}$ [Yu *et al.*, 2006, and references therein]. Among those studies of clear-sky DRE, only Loeb and Manalo-Smith [2005] provided all-sky DRE over ocean of -1.6 to -2.0 Wm^{-2} .

[3] Estimation of aerosol DRF from satellite measurements is more challenging because current satellite sensors do not have the capability of discriminating anthropogenic aerosols from natural aerosols. To circumvent this limitation, two approaches have been commonly used to estimate DRF. First, fine-mode fraction of aerosol optical depth (AOD; τ)

¹NASA Langley Research Center, Hampton, VA, USA.

²Goddard Space and Flight Center, Greenbelt, MD, USA.

³Science Systems and Applications Inc., Hampton, VA, USA.

Corresponding author: Dr. Wenying Su, MS 420, Science Directorate, NASA Langley Research Center, Hampton, VA 23681, USA. (Wenying.Su-1@nasa.gov)

© 2012. American Geophysical Union. All Rights Reserved.
2169-897X/13/2012JD018294

derived from satellite measurements has been used to quantify anthropogenic aerosols (since anthropogenic aerosols are predominately submicron). This approach has been used only over oceans because satellite retrievals of fine-mode fraction over land has a much larger uncertainty than over ocean. For example, *Kaufman et al.* [2005] estimated DRF over clear ocean using fine-mode fraction of τ retrieved from Moderate Resolution Imaging Spectroradiometer (MODIS). By combining estimates of the anthropogenic aerosol forcing efficiency and aerosol DRE over clear ocean, they calculated the clear-sky DRF as $-1.4 \pm 0.4 \text{ Wm}^{-2}$. However, MODIS retrievals of the fine-mode fraction are systematically greater than the submicron fraction obtained from suborbital measurements [*Anderson et al.*, 2005].

[4] The second approach combines satellite retrievals with model-simulated aerosol components. *Bellouin et al.* [2005, 2008] used fine-mode fraction of τ from MODIS to approximate anthropogenic fraction over ocean and used five models to assess the anthropogenic fraction over land. The anthropogenic fraction is 0.35 over South America and is 0.56 over North America from these model simulations. They estimated that the global clear-sky aerosol DRF is -1.9 or -1.3 Wm^{-2} depending upon which MODIS collections (4 or 5) are used. A more complete list of clear-sky aerosol DRF estimates is summarized by *Yu et al.* [2009].

[5] As noted in *Yu et al.* [2009] (Table 2.7), there are substantial differences between clear-sky DRF derived from satellite observations and model simulations. Over ocean, the mean satellite-based clear-sky DRF is $-1.1 \pm 0.37 \text{ Wm}^{-2}$, which is about a factor of 2 stronger than that from model simulations. Clear-sky DRFs are more negative over land than over ocean for both satellite-based estimates and model simulations because of the larger anthropogenic aerosol fractions over land than over ocean. Over land, the satellite-based clear-sky DRF estimates range from -1.8 to -3.3 Wm^{-2} , and the model-simulated mean DRF is -1.1 Wm^{-2} . On a global scale (60°N – 60°S), the satellite-based estimates of clear-sky DRF range from -0.9 to -1.9 Wm^{-2} , while the model-simulated mean DRF is -0.8 Wm^{-2} .

[6] Only a few satellite-based studies estimated the all-sky DRF. *Bellouin et al.* [2005] simply scaled the clear-sky DRF and uncertainty by clear-sky fraction (1 minus cloud fraction) and derived the global all-sky DRF to be $-0.8 \pm 0.1 \text{ Wm}^{-2}$; hence, they implicitly assume that aerosols do not contribute to DRF in cloudy regions. However, this assumption is only valid if the cloud albedo is unity and there are no aerosols above clouds [*Liao and Seinfeld*, 1998]; and if there are absorbing aerosols above the clouds, high reflection of the clouds will cause aerosol DRF to switch sign from negative to positive [*Chylek and Coakley*, 1974; *Charlock and Sellers*, 1980; *Haywood and Shine*, 1995; *Podgorny and Ramanathan*, 2001; *Bellouin et al.*, 2008; *Chand et al.*, 2009]. Furthermore, scaling clear-sky uncertainty to all-sky uncertainty assumes that uncertainties in cloud properties do not contribute to the all-sky DRF uncertainty, which oversimplifies the problem and substantially underestimates the all-sky DRF uncertainty [*Loeb and Su*, 2010].

[7] A method that improves upon the *Bellouin et al.* [2005] technique was introduced by *Chung et al.* [2005]. They calculated clear- and all-sky anthropogenic DRF by incorporating monthly mean aerosol and cloud properties derived from satellites, ground-based observations, and a chemical transport

model into a radiative transfer model. In their calculation, aerosol profiles in the boundary layer were assumed to be uniform from surface to 3.4 km in the tropics and uniform from surface to 2 km in the extratropics. Aerosol density is assumed to decrease exponentially above the boundary layer for the baseline case. The global annual mean all-sky DRF was -0.35 Wm^{-2} for the baseline aerosol profile case, but changing the vertical profiles of aerosols altered the DRF by $\pm 0.25 \text{ Wm}^{-2}$. Although *Chung et al.* [2005] considered clouds explicitly in their DRF estimation, calculating DRF using monthly mean aerosol and cloud properties is not ideal, since both aerosols and clouds change on a much shorter temporal scale. Additionally, they only considered two types of aerosols profiles (tropics and extratropics) in their calculation, which are not representative of the regional and seasonal aerosol vertical distributions.

[8] The satellite-based all-sky DRF estimates differ significantly from model simulations provided by the AeroCom aerosol modeling intercomparison project [*Schulz et al.*, 2006]. The average all-sky DRF simulated by nine AeroCom global models is $-0.22 \pm 0.16 \text{ Wm}^{-2}$. Based upon both measurement and model results, the Intergovernmental Panel on Climate Change's (IPCC's) Fourth Assessment Report (AR4) listed the all-sky DRF as -0.5 Wm^{-2} , with an uncertainty of 0.4 Wm^{-2} at the 90% confidence level [*Forster et al.*, 2007]. Recently, *Myhre* [2009] argued that difference between satellite-based and model-based DRF is due to the inconsistency in pre-industrial aerosol optical properties. Using consistent pre-industrial aerosol properties reduces this difference, but this reduction in difference is not equivalent to reduction in uncertainty because his satellite-based and model-based DRF estimates are not independent of one another.

[9] In this study, we combine 3-hourly cloud properties from Clouds and Earth's Radiant Energy System (CERES) Synoptic Radiative Fluxes and Clouds (SYN) product with two aerosol data sets to calculate the clear-sky and all-sky aerosols DREs. The first aerosol data set is based upon MODIS aerosol retrieval and an aerosol assimilation model [Model for Atmospheric Transport and Chemistry (MATCH)], hereafter refer to as MODIS/MATCH. MATCH does not distinguish between anthropogenic and natural aerosols; thus, we cannot determine aerosol DRF from this data set. The other aerosol data set is based upon the Goddard Chemistry Aerosol Radiation and Transport (GOCART), which does not assimilate aerosol measurements but predicts the anthropogenic and natural components of aerosols. We therefore can calculate the ratio of DRF to DRE based upon GOCART aerosol classifications. We then apply this ratio to DRE calculated using MODIS/MATCH aerosols to partition it into DRF, assuming the anthropogenic fraction from GOCART is representative.

2. Data and Methodology

2.1. Cloud Properties

[10] The 3-hourly CERES SYN product (Edition 2) provides merged cloud properties based upon MODIS [*Minnis et al.*, 2008, 2011] and geostationary satellite retrievals [*Minnis et al.*, 1995; *Doelling et al.*, 2013]. To ensure consistent cloud property retrievals from MODIS and geostationary satellite, each geostationary imager is calibrated against

MODIS over its entire life span using a ray-matching calibration technique [Minnis *et al.*, 2002], and the same cloud retrieval algorithm is used for geostationary imagers and MODIS. The retrieved cloud properties include cloud fraction, cloud optical depth, cloud top and base pressure, liquid particle radius, and ice particle diameter. These properties are allocated in four layers in the SYN product (below 700 hPa, 700–500 hPa, 500–300 hPa, and above 300 hPa).

2.2. Aerosol Properties

[11] We use aerosol properties from two data sets. The first aerosol data set relies on aerosol optical depths (τ) retrieved from MODIS [Remer *et al.*, 2005] when they are available; otherwise, τ from the Model for Atmospheric Transport and Chemistry (MATCH) aerosol assimilation [Collins *et al.*, 2001] are used. MATCH assimilates MODIS τ (Collection 4) based upon optimal interpolation approach, which modifies modeled fields to match observations in a manner consistent with uncertainties in the modeled and observed τ . Thus, aerosol optical depths in MODIS/MATCH data are constrained, to a large extent, by MODIS retrievals. Aerosol compositions are inferred from the MATCH model because MODIS retrieval does not provide information on composition. MATCH simulates aerosol species of sulfate, mineral dust, sea salt, black carbon (BC), and organic carbon (OC). However, MATCH does not separate anthropogenic from natural aerosols; it is not possible to derive DRF from this aerosol data set alone.

[12] The second aerosol data set is from GOCART, which uses assimilated meteorological fields from the Goddard Earth Observing System Data Assimilation System (GEOS DAS). GOCART simulates major aerosol types of sulfate, dust, BC, OC, sea salt, and the precursor gas species of SO₂ and dimethylsulfide (DMS). The model accounts for emissions from anthropogenic, biomass burning, biogenic, volcanic sources, wind-blown dust, and sea salt. Aerosol particle sizes from 0.01 to 10 μm are simulated with parameterized hygroscopic growth, which is a function of ambient relative humidity. Details of the GOCART model are described in previous publications [Chin *et al.*, 2002, 2004, 2007, 2009; Ginoux *et al.*, 2001, 2004]. The major difference between GOCART and MATCH is that GOCART does not assimilate satellite retrievals of aerosols.

[13] Aerosol produced from pollution, biomass burning, and natural sources are labeled in the GOCART model, and it therefore diagnostically separates anthropogenic from natural aerosols. The natural aerosols include dust, sea salt, sulfate from volcanic eruption, and OC from biogenic sources. The anthropogenic aerosols include sulfate, BC, and OC from fossil fuel/biofuel combustions, ship and aircraft emissions, and biomass burning. Therefore, we can derive both aerosol DRE and DRF from GOCART aerosols.

2.3. Clear-sky and All-sky Aerosol Direct Radiative Effect and Forcing Calculations

[14] We use 3-hourly cloud properties and daily MODIS/MATCH aerosol properties in the Fu-Liou correlated- k radiative transfer code [Fu and Liou, 1992, 1993; Rose and Charlock, 2002] to calculate 3-hourly fluxes at the TOA and surface. The Fu-Liou model includes optical properties (extinction, single-scattering albedo, and asymmetry parameter) for different aerosol species. Optical properties for dust aerosols are adopted from Dubovik *et al.* [2002]; Sinyuk

et al. [2003], and optical properties for BC, OC, sulfate, and sea-salt aerosols are adopted from Optical Properties of Aerosols and Clouds [OPAC, Hess *et al.*, 1998]. Other input datasets include temperature and humidity profiles from GEOS (version 4), daily global ozone profiles from Stratosphere Monitoring Ozone Blended Analysis (SMOBA) [Yang *et al.*, 1999], ocean spectral albedos [Jin *et al.*, 2004], and satellite retrieved broadband surface albedos over land and snow using a priori surface spectral characteristics (which agree with MODIS land surface albedos to within 2% [Rutan *et al.*, 2009]). The radiative transfer calculation provides fluxes for clear-sky no aerosol, clear-sky, all-sky no-aerosol, and all-sky conditions. Clear-sky and all-sky aerosol DRE can be calculated from these fluxes:

$$DRE_{clr}^m = F_{clr,t}^m - F_{clr,p} \quad (1)$$

and

$$DRE_{all}^m = F_{all,t}^m - F_{all,p}, \quad (2)$$

where F is the net flux (downwelling minus upwelling) at TOA or surface, $F_{clr,t}^m$ is for clear-sky with total aerosols from MODIS/MATCH, $F_{clr,p}$ is for clear-sky without aerosols, $F_{all,t}$ is for all-sky with total aerosols from MODIS/MATCH, and $F_{all,p}$ is for all-sky without aerosols. Here superscript m denotes variables calculated using MODIS/MATCH aerosols.

[15] Since MATCH does not separate anthropogenic from natural aerosols, we cannot derive aerosol DRF from MODIS/MATCH alone. GOCART, on the other hand, differentiates anthropogenic from natural aerosols. Assuming the anthropogenic fraction from GOCART is reliable, we use the anthropogenic aerosol components prescribed by the GOCART model to partition clear-sky and all-sky DRE derived from MODIS/MATCH aerosols into clear-sky and all-sky DRF (Figure 1). However, if GOCART underestimates the anthropogenic fraction, then our current estimates of DRF would be too large. Although the following discussion focuses on deriving the all-sky components, the corresponding clear-sky components are obtained at the same time.

[16] **Run 1:** We first run the Fu-Liou model using daily total aerosol components from GOCART and the same 3-hourly cloud properties and surface albedo as for the MODIS/MATCH aerosol runs. Daily aerosol optical depths and vertical profiles of different species from GOCART (including sulfate, dust, BC, OC, and sea salt) are used in the Fu-Liou model to calculate the all-sky 3-hourly fluxes with GOCART total aerosols ($F_{all,t}^g$). GOCART all-sky aerosol DRE (DRE_{all}^g) is then calculated by the following:

$$DRE_{all}^g = F_{all,t}^g - F_{all,p}, \quad (3)$$

where $F_{all,p}$ is the all-sky without aerosol net flux, and it is equivalent to $F_{all,p}$ in equation (2). Here superscript g denotes variables calculated using GOCART aerosols.

[17] **Run 2:** The second time we run Fu-Liou model, we use only natural aerosol components from GOCART (including sulfate, dust, OC, and sea salt) and the same 3-hourly cloud properties and surface albedo. This produces the all-sky 3-hourly flux associated with natural aerosols

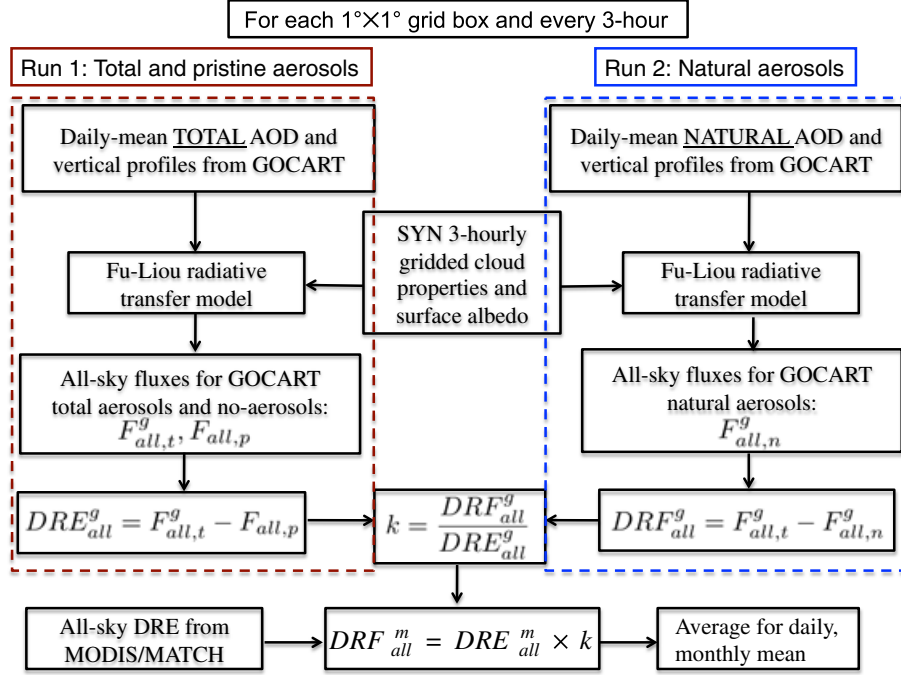


Figure 1. Flowchart illustrating the derivation of all-sky aerosol direct radiative forcing by combining the cloud properties from Clouds and Earth’s Radiant Energy System (CERES) Synoptic Radiative Fluxes and Clouds (SYN) product with total and natural aerosol compositions from the Goddard Chemistry Aerosol Radiation and Transport (GOCART) model. k is the partition ratio of aerosol direct radiative forcing (DRF) to aerosol direct radiative effect (DRE) derived from the GOCART aerosol composition for every 1° by 1° grid box every 3 h.

$(F_{all,n}^g)$. GOCART all-sky aerosol direct radiative forcing (DRF_{all}^g) is calculated by the following:

$$DRF_{all}^g = F_{all,t}^g - F_{all,n}^g. \quad (4)$$

[18] **Derive k :** Thus, we can derive the ratio of direct radiative forcing to direct radiative effect associated with the natural and anthropogenic aerosol components in GOCART for every 1° × 1° grid box at every time step(3 h):

$$k = \frac{DRF_{all}^g}{DRE_{all}^g} = \frac{F_{all,t}^g - F_{all,n}^g}{F_{all,t}^g - F_{all,p}^g}. \quad (5)$$

[19] We then apply this partition ratio to the all-sky aerosol DRE_{all}^m calculated using MODIS/MATCH to derive the forcing component:

$$DRF_{all}^m = k \times DRE_{all}^m. \quad (6)$$

[20] The DRE and DRF within the atmosphere (atmospheric absorption) are calculated as the difference between TOA and surface components. These 3-hourly DRE and DRF are then averaged to derive the daily, monthly, and annual mean DRE and DRF at the TOA, within the atmosphere, and at the surface. Here we use data of 2004 and provide seasonal and annual results of aerosol DRE and DRF. The four seasons are December–February (DJF), March–May (MAM), June–August (JJA), and September–November (SON). Recall Chung *et al.* [2005] used the monthly mean aerosol and cloud properties and two aerosol vertical profiles in their all-

sky DRF calculations. The fine temporal resolutions of aerosol and cloud properties together with the more realistic aerosol profiles used in our study are expected to produce more accurate DRE and DRF than those presented in Chung *et al.* [2005].

[21] An alternative approach could partition the present-day aerosol optical depth in MODIS/MATCH using the anthropogenic fraction prescribed by GOCART (instead of using the k value discussed above). GOCART provides anthropogenic fractions for sulfate, BC, and OC aerosols, which can then be applied to these aerosol components simulated by MATCH, and thereby derive the natural components in MODIS/MATCH. To quantify the difference in DRF_{all}^m from these two methods, we apply the alternative method to 1 July. The daily mean DRF_{all}^m is -0.51 and -0.53 Wm^{-2} from the alternative approach and the method that we adopted here (equation 6). Thus, DRF from these two methods are within about 4% of each other.

3. Results

3.1. Aerosol Optical Properties

[22] We rely on two aerosol data sets (MODIS/MATCH and GOCART) to calculate the aerosol DRE and DRF. Since aerosol DRF is highly sensitive to aerosol optical depth and single-scattering albedo [Loeb and Su, 2010], we compare these two properties here. Seasonal aerosol optical depths at $0.55 \mu\text{m}$ in MODIS/MATCH (τ_m) are shown in Figure 2. To highlight the aerosol optical depth differences between MODIS/MATCH and the GOCART model (τ_g), we show the seasonal τ differences ($\Delta\tau = \tau_m - \tau_g$) in Figure 3. The

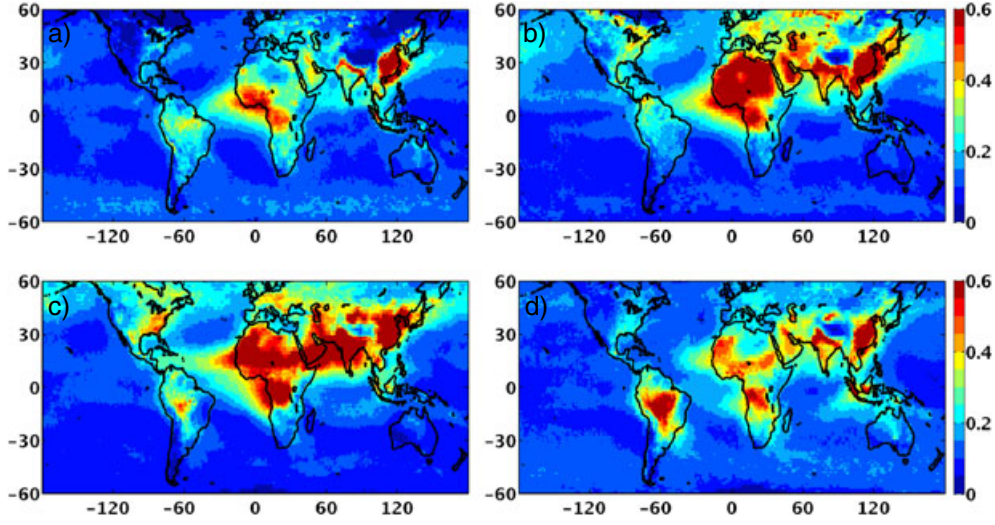


Figure 2. Global distributions of seasonal aerosol optical depth in 2004 from Moderate Resolution Imaging Spectroradiometer/Model for Atmospheric Transport and Chemistry (MODIS/MATCH) for (a) DJF, (b) MAM, (c) JJA, and (d) SON.

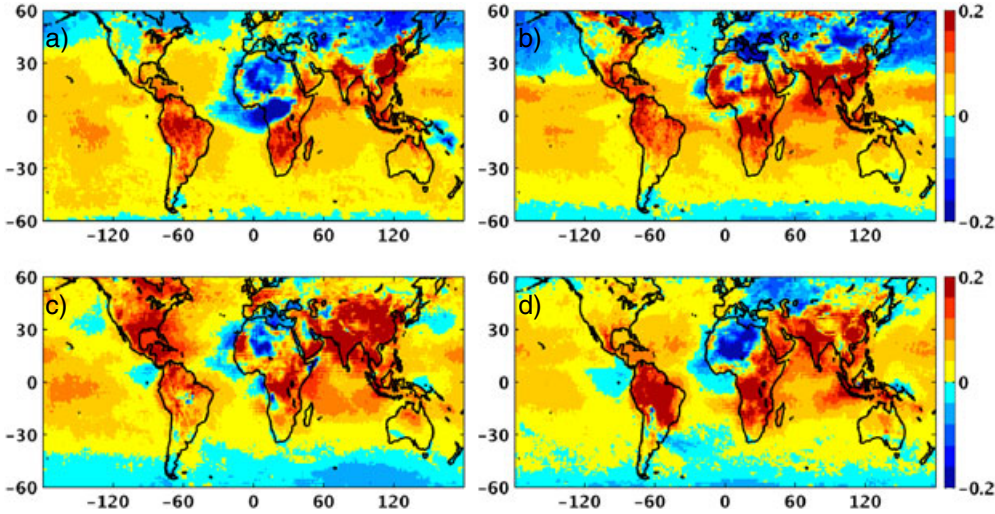


Figure 3. Global distributions of seasonal aerosol optical depth difference in 2004 between MODIS/MATCH and the GOCART model for (a) DJF, (b) MAM, (c) JJA, and (d) SON.

seasonal distributions of $\Delta\tau$ reveal that τ_g are generally smaller than τ_m . This is particularly true over South America, southern Africa, eastern China, and India. For example, τ_g are smaller than τ_m by about 50% over South America and southern Africa. However, τ_g are generally larger than τ_m over northern Africa, Eastern Europe, and northern Pacific Ocean during the dust outbreak season (MAM) by about 10–20%. Global (60°N–60°S, same hereafter) seasonal and annual mean τ_m and τ_g (Table 1) show that the differences range from 0.03 in DJF to 0.05 in JJA. On the annual mean basis, τ_g is smaller than τ_m by 0.03 and 0.06 over the global ocean and land, respectively.

[23] Aerosol optical depths from MODIS/MATCH are validated against Aerosol Robotic Network (AERONET) measurements (Figure 4a). The locations of the AERONET sites used for this validation are mostly over land (see Figure 4 in *Chin et al.* [2009]). The monthly mean τ from MODIS/MATCH is greater than that from AERONET by about

38%, which agrees with the MODIS validation results over land [*Remer et al.*, 2005]. Similar validation for GOCART indicates that GOCART underestimates τ by about 8% [*Chin et al.*, 2009]. Validation of MODIS AOD over ocean against oceanic AERONET sites indicates that the agreement is within 1% [*Remer et al.*, 2005].

[24] Aerosols in these two data sets have different compositions. We show seasonal single-scattering albedo at 0.55 μm of MODIS/MATCH aerosols (ω_m) in Figure 5. Large absorption (small ω_m) occurs over biomass burning regions, industrial regions, and dust regions. These absorbing aerosols are transported to the adjacent oceans resulting in relatively low ω_m . The single-scattering albedo differences between MODIS/MATCH and GOCART ($\Delta\omega = \omega_m - \omega_g$) are shown in Figure 6. Although global mean ω_m is only about 0.01–0.02 larger than ω_g (aerosols in GOCART are more absorbing, see Table 1), some regional differences are up to 0.05.

Table 1. Global (60°N–60°S) seasonal and annual mean aerosol optical depths and single-scattering albedos from Moderate Resolution Imaging Spectroradiometer/Model for Atmospheric Transport and Chemistry (MODIS/MATCH) (τ_m , ω_m) and from Goddard Chemistry Aerosol Radiation and Transport (GOCART) (τ_g , ω_g), and the anthropogenic fractions predicted by GOCART (η)¹

	DJF	MAM	JJA	SON	Annual				
	Global				Global	Ocean	Land	NH	SH
τ_m	0.15	0.19	0.20	0.17	0.18	0.14	0.28	0.23	0.13
τ_g	0.12	0.15	0.15	0.13	0.14	0.11	0.22	0.19	0.09
ω_m	0.97	0.97	0.97	0.96	0.97	0.97	0.95	0.97	0.97
ω_g	0.96	0.96	0.95	0.95	0.96	0.96	0.94	0.96	0.96
η (%)	41.8	34.5	41.5	47.3	41.2	37.7	44.2	40.3	42.1

¹Annual mean τ_m , τ_g , ω_m , ω_g , and η are also listed separately over global ocean, land, Northern Hemisphere (NH), and Southern Hemisphere (SH).

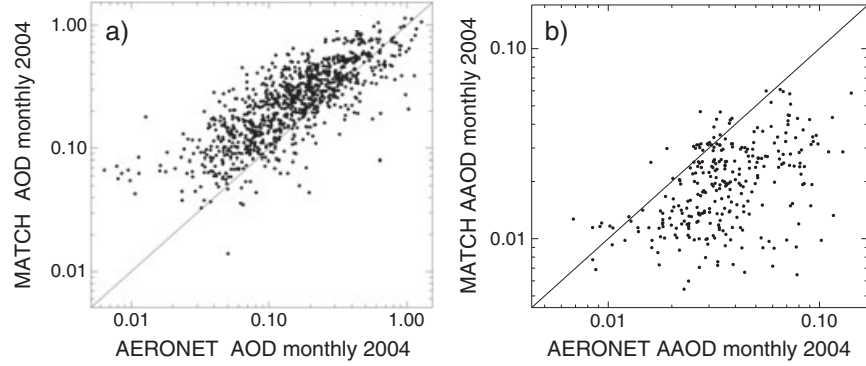


Figure 4. Comparisons of (a) aerosol optical depth and (b) absorbing aerosol optical depth at 0.55 μm between Aerosol Robotic Network (AERONET) and MATCH for 2004. Each point represents the monthly average. Locations of the AERONET sites are shown in Figure 4 of (Chin *et al.*, 2009).

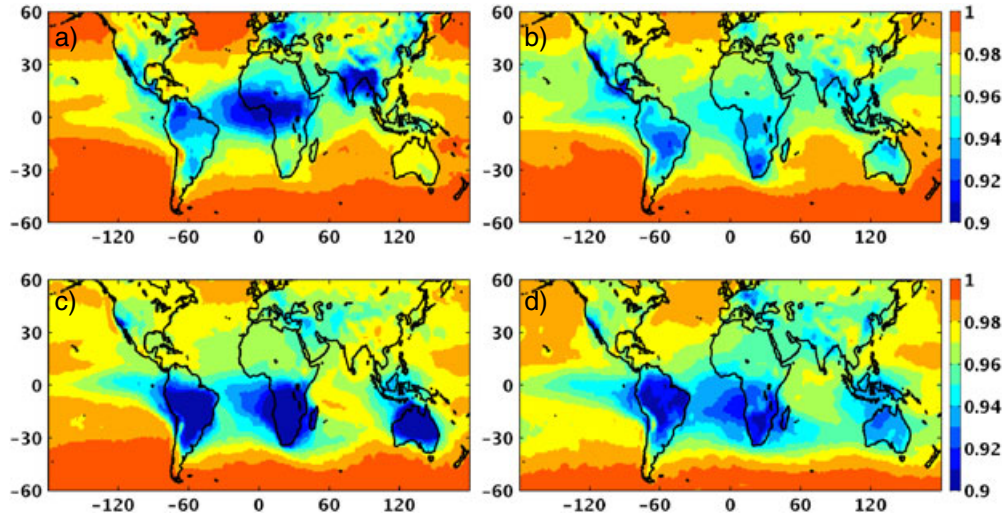


Figure 5. Global distributions of seasonal aerosol single-scattering albedo in 2004 from MODIS/MATCH for (a) DJF, (b) MAM, (c) JJA, and (d) SON.

GOCART aerosols are more absorbing than MODIS/MATCH aerosols over Southeast Asia, midlatitude Pacific Ocean, Indian Ocean, and southern Africa but are less absorbing over South America, tropical Pacific Ocean, and Western Europe.

[25] We validated the absorbing aerosol optical depth ($\tau^{abs} = \tau \times (1 - \omega)$) against the AERONET retrievals. The monthly mean τ^{abs} from MODIS/MATCH is smaller than τ^{abs} from AERONET retrievals by about 48% (Figure 4b).

Similar validation indicates that τ^{abs} from GOCART is on average smaller than τ^{abs} from AERONET by 12% [Chin *et al.*, 2009]. Assuming these AERONET validation results are applicable to global land regions, insufficient absorption in both aerosol datasets indicates an overestimation of the cooling effect of TOA DRE/DRF over land.

[26] As we mentioned earlier, optical properties of “water-soluble” species in OPAC are used to approximate the optical

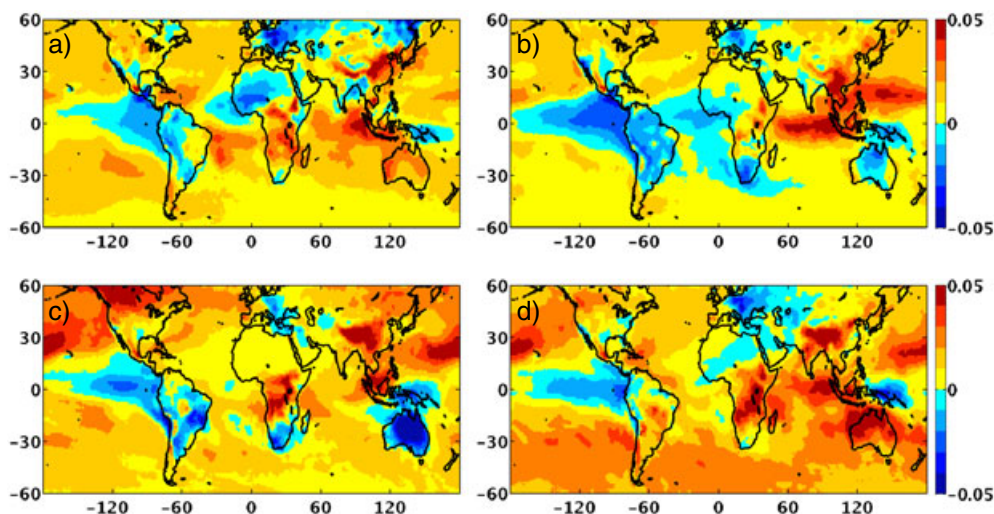


Figure 6. Global distributions of seasonal aerosol single-scattering albedo difference in 2004 between MODIS/MATCH and the GOCART model for (a) DJF, (b) MAM, (c) JJA, and (d) SON.

properties of OC. Thus, the dry complex refractive index of our organic aerosol species is $1.53-0.006i$ at the $0.550\ \mu\text{m}$ wavelength, and the single-scatter albedo varies with relative humidity from $0.96-1.0$. Although an imaginary refractive index of 0.006 does not result in a highly absorbing OC aerosol at this wavelength, we note that this is the upper end of values implemented for OC in seven aerosol transport models surveyed by *Kinne et al.* [2003]. It is also consistent with the *Kanakidou et al.* [2005] review, who quote single-scattering albedo (SSA) = $0.94-1.0$ from various sources. *Chakrabarty et al.* [2010] also obtained SSAs from $0.96-0.98$ at $532\ \text{nm}$ for brown carbon tar balls generated with Ponderosa Pine duff and Alaskan tundra duff. Additionally, [*Hoffer et al.*, 2006] isolated humic-like substance from biomass burning aerosols in the Amazon basin and deduced imaginary refractive indices of $0.0016-0.0019$ and SSA values of $0.98-0.99$ at $0.532\ \mu\text{m}$.

[27] However, some recent measurements indicate that OC can be significantly more absorbing than the OPAC water-soluble aerosol species at midvisible wavelengths. For instance, *Kirchstetter et al.* [2004] deduced an imaginary refractive index of $k=0.03$ for OC extracted from wood burning smoke and South African biomass smoke. Even more startling, *Alexander et al.* [2008] used transmission electron microscopy to observe imaginary refractive indices as high as 0.27 and SSAs as low as 0.44 for large brown carbon tar balls ($\sim 0.2\ \mu\text{m}$ diameter) in the East Asian Outflow. Separation of OC absorption from BC absorption is generally difficult, so optical measurements that isolate OC from BC are rare. Biomass smoke is often associated with OC, but the absorption of biomass burning is sensitive to the fuel type and the OC/BC ratio (absorption increases as the OC/BC ratio decreases; *Schnaiter et al.* [2006]; *Levin et al.* [2010]). Thus, the *Kirchstetter et al.* [2004] and *Alexander et al.* [2008] refractive indices do not necessarily represent an appropriate global OC climatology.

[28] Additionally, we rely on GOCART to prescribe the anthropogenic fraction (η), which is defined as the ratio of anthropogenic τ_g to total τ_g . GOCART predicts high η over populated continents and over biomass burning regions of South America and southern Africa (Figure 7). Substantial

anthropogenic influences are also seen over North Pacific, North Atlantic, Arabian Sea, and Bay of Bengal because of the outflow from industrial pollution and over South Atlantic from biomass burning. The highest η occurs during SON and the smallest during MAM (Table 1). This is because SON is the strongest biomass burning season, while biomass burning in MAM is the weakest. The global annual mean η is 41% from the GOCART model, with greater anthropogenic impact over land (44%) than over ocean (38%).

[29] The aerosol vertical distributions from GOCART and MATCH differ from that derived from Cloud-Aerosol Lidar with Orthogonal Polarization (CALIPSO) layer product. Both models generally place aerosols at higher altitude than CALIPSO retrievals [*Yu et al.*, 2010; *Koffi et al.*, 2012]. For example, mean extinction heights of GOCART and MATCH are higher than those from CALIPSO by about 0.3 and $0.5\ \text{km}$ over southern Africa and by about 0.5 and $0.9\ \text{km}$ over South America [*Koffi et al.*, 2012]. Note that CALIPSO does not have the capability to differentiate absorbing aerosols from scattering aerosols. If we assume that the vertical distribution differences seen in total aerosols are representative for the absorbing components, then relying on the aerosol vertical distributions prescribed by the models will overestimate the warming effects of the absorbing aerosols and therefore underestimate the total cooling effect of aerosols.

3.2. Aerosol Direct Radiative Effect

[30] Clear-sky aerosol DREs are calculated based upon MODIS/MATCH and GOCART aerosols. All-sky aerosol DRE for these two aerosol data sets are calculated using 3-hourly cloud properties from the CERES SYN product.

3.2.1. Clear-sky Aerosol Direct Radiative Effect

[31] Table 2 summarizes the clear-sky DRE from MODIS/MATCH (DRE_{clr}^m) and from the GOCART model (DRE_{clr}^g). Global mean DRE_{clr}^m are greater than DRE_{clr}^g by about 28% ($1.3\ \text{Wm}^{-2}$), 12% ($0.4\ \text{Wm}^{-2}$), and 22% ($1.6\ \text{Wm}^{-2}$) at the TOA, within the atmosphere, and at the surface. Largest differences occur over the Southern Hemisphere (SH). For

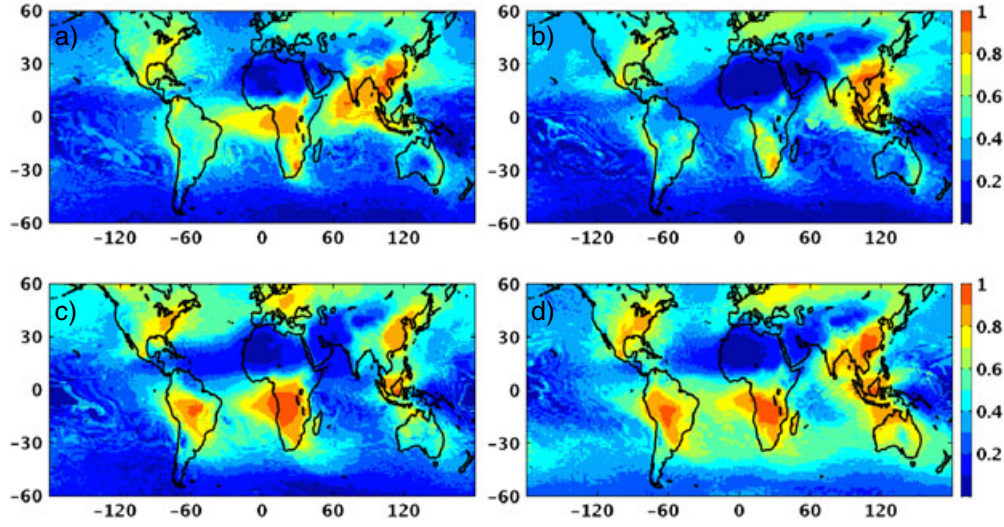


Figure 7. Global distributions of seasonal anthropogenic fraction in 2004 predicted by the GOCART model for (a) DJF, (b) MAM, (c) JJA, and (d) SON.

Table 2. Annual mean clear-sky direct aerosol radiative effect (Wm^{-2}) at the top of atmosphere, within the atmosphere, and at the surface derived using MODIS/MATCH aerosols (DRE_{clr}^m) and GOCART aerosols (DRE_{clr}^g) over the globe, ocean, land, Northern Hemisphere (NH), and Southern Hemisphere (SH)¹

	Global		Ocean		Land		NH		SH	
	DRE_{clr}^m	DRE_{clr}^g	DRE_{clr}^m	DRE_{clr}^g	DRE_{clr}^m	DRE_{clr}^g	DRE_{clr}^m	DRE_{clr}^g	DRE_{clr}^m	DRE_{clr}^g
TOA	−5.76	−4.49	−5.23	−4.03	−7.18	−5.71	−7.03	−6.07	−4.52	−2.96
Atmos	3.37	3.01	1.96	1.94	7.06	5.83	4.27	4.21	2.48	1.83
Sfc	−9.13	−7.50	−7.19	−5.97	−14.23	−11.54	−11.30	−10.28	−7.00	−4.79

TOA, top of the atmosphere.

¹Mean values are calculated from 60°N to 60°S.

both DRE_{clr}^m and DRE_{clr}^g , the aerosol DREs over land are greater than those over ocean, and aerosol DREs over Northern Hemisphere (NH) are greater than those over SH because large aerosol sources exist over NH land [Charlson *et al.*, 1992]. It is not surprising to see that DRE_{clr}^m is greater than DRE_{clr}^g , since τ_m is greater than τ_g (Table 1). Additionally, the aerosol absorptions used in these two data sets are also different (Table 1), which could also contribute a secondary effect to the differences between DRE_{clr}^m and DRE_{clr}^g .

[32] Over clear ocean, our observational-based TOA DRE_{clr}^m is -5.2 Wm^{-2} , which is in good agreement with the mean DRE of -5.5 Wm^{-2} from published observational-based estimations [Yu *et al.*, 2009, and references therein]. The surface DRE_{clr}^m is -7.2 Wm^{-2} , while other observational-based surface DRE ranges from -7.7 to -11.1 Wm^{-2} [Yu *et al.*, 2009]. Interestingly, the lower end of the surface DRE (-7.7 Wm^{-2}) from Bellouin *et al.* [2003] was derived using AERONET retrievals of aerosol absorption as a constraint. Other estimates which produce large surface cooling [Yu *et al.*, 2004, 2006] rely on OPAC for aerosol absorption. Numerous studies have pointed out that dust absorption in the OPAC model is overestimated [Kaufman *et al.*, 2001; Dubovik *et al.*, 2002; Sinyuk *et al.*, 2003; Catrall *et al.*, 2003], and when OPAC dust absorption is replaced by AERONET dust absorption, the surface cooling is reduced by 0.9 Wm^{-2} [Yu *et al.*, 2004].

[33] Over clear land, our observational-based DRE_{clr}^m shows much stronger cooling effects than those summarized in Yu *et al.* [2006] at the TOA and the surface. However, the atmospheric absorptions are comparable. The annual mean τ_m over land (Table 1) is larger than the aerosol optical depths (range from 0.19 to 0.23) from Yu *et al.* [2006], and our AERONET-based dust model is less absorptive than the OPAC dust model used in Yu *et al.* [2006]. The combination of smaller τ and more absorbing aerosols in Yu *et al.*, [2006] than in our study results in comparable atmospheric absorptions. If the validations over land AERONET sites (mostly over North America and Europe) are representative for global land, the GOCART DRE over land would be more reliable. Aerosol optical depths from MODIS over ocean agree fairly well with the oceanic AERONET sites [Remer *et al.*, 2005]. If this is representative over global ocean, the MODIS DRE over ocean is more accurate.

[34] Global distributions of clear-sky DREs for JJA 2004 derived using MODIS/MATCH aerosols are shown in Figures 8a–8c. The clear-sky TOA DREs (Figure 8a) indicate large coolings over high τ_m regions (Figure 2c). Dust outbreaks and biomass burning in Africa result in TOA cooling over -10 Wm^{-2} and extend over the Atlantic Ocean to Central America. We also observe clear-sky TOA DREs as large as -20 Wm^{-2} over India, the Arabian Sea, and eastern China. In some regions of northern Pacific, aerosol DRE is

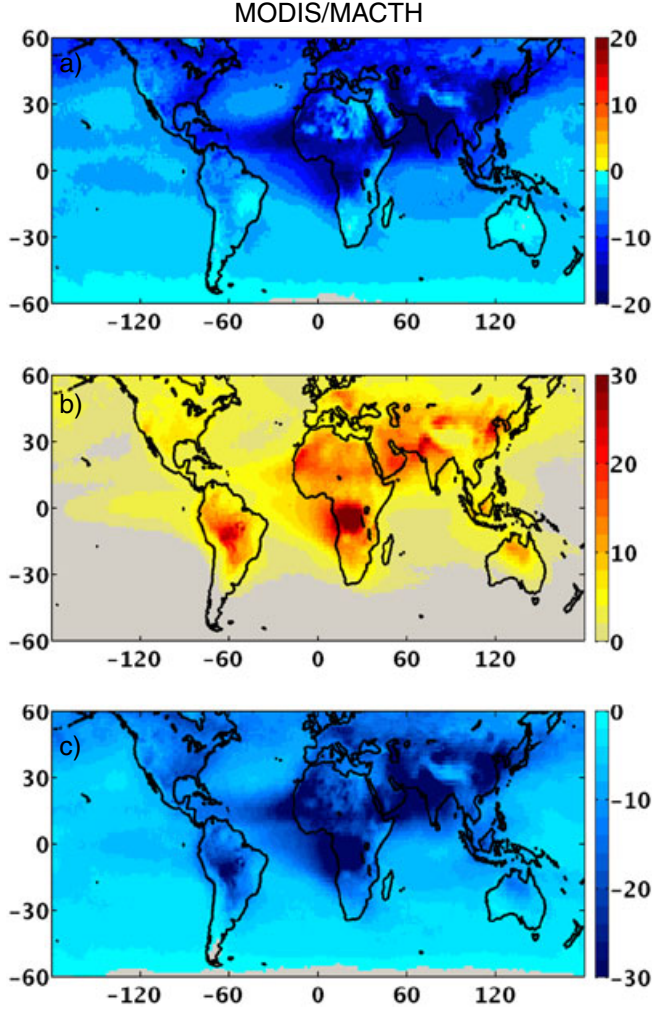


Figure 8. Global distributions of clear-sky aerosol direct radiative effect (Wm^{-2}) from MODIS/MATCH aerosols (a) at the top of the atmosphere (TOA) (gray color indicates DRE is within $\pm 0.25 \text{ Wm}^{-2}$), (b) within the atmosphere (gray color indicates atmospheric absorption is less than 1 Wm^{-2}), and (c) at the surface (gray color indicates surface cooling is less than 1 Wm^{-2}) for JJA 2004.

up to -10 Wm^{-2} because of the transport of Asian aerosols. The global mean clear-sky TOA aerosol DRE is -6.3 Wm^{-2} during JJA. The surface aerosol DRE is negative (cooling effect, Figure 8c), and its distribution is very similar to that of TOA DRE. The global mean clear-sky surface DRE is -10.2 Wm^{-2} for this season. Within the atmosphere, large aerosol absorptions over biomass burning regions of Africa and South America, over heavily polluted regions of eastern China and India, and over dust outbreak regions of Africa and the Middle East all result in atmospheric warming of over 10 Wm^{-2} (Figure 8b). The global mean clear-sky atmospheric aerosol absorption is 3.9 Wm^{-2} .

3.2.2. All-sky Aerosol Direct Radiative Effect

[35] The all-sky components of the aerosol DRE are listed in Table 3. We first discuss clouds' effect on DRE by comparing the all-sky and clear-sky DRE and explain the deficiency of

the scaling method. We then illustrate the aerosols' effect on all-sky DRE by comparing the distributions of all-sky DRE derived from MODIS/MATCH and GOCART aerosols.

[36] The presence of clouds reduces the global TOA aerosol DRE, and the percentage reduction is greater over ocean than over land. This is because the cloud fraction over ocean is about 5–15% greater than over land [Stubenrauch *et al.*, 2009]. Globally, the DRE_{all}^m and DRE_{all}^g are about 53% and 43% of their clear-sky components. Clouds reduce the clear-sky DRE by different percentage because the aerosol vertical distribution and absorption are different in these two aerosol data sets. Recall that some studies approximate the all-sky DRE by scaling the clear-sky DRE with clear-sky fraction ($DRE_{scl} = DRE_{clr} \times (1 - f)$, f is the cloud fraction). For 2004, the global annual mean $f = 66\%$. If we use the scaling method, the all-sky DRE would be about 34% of the clear-sky DRE. Therefore, the scaling method would underestimate the all-sky DRE by 9–19% ($0.7\text{--}1.0 \text{ Wm}^{-2}$, depending on the aerosol inputs).

[37] Furthermore, the presence of clouds also changes the distribution of DRE. In stark contrast to clear-sky TOA DRE_{clr}^m (Figure 8a), the all-sky DRE_{all}^m (Figure 9a) is positive over biomass burning regions of southern Africa and South America. This is because when absorbing aerosols are over highly reflective clouds, the radiative effect of absorbing aerosols changes from cooling to warming [Chylek and Coakley, 1974; Charlock and Sellers, 1980; Haywood and Shine, 1995; Podgorny and Ramanathan, 2001; Bellouin *et al.*, 2008; Chand *et al.*, 2009]. The all-sky TOA DRE_{all}^m shows a smaller cooling effect than clear-sky DRE_{clr}^m over dust outbreak regions of Africa and Middle East and over heavily polluted regions of India and eastern China. The global mean all-sky TOA aerosol DRE is -3.4 Wm^{-2} , which is about half of the clear-sky TOA DRE.

[38] Comparing the distributions of TOA DRE_{all}^m (explicitly account for clouds in the atmosphere) and DRE_{scl}^m (simply scale DRE_{clr}^m by clear-sky fraction), we note that over regions where aerosols are predominately absorbing, DRE_{all}^m indicates warming effect, whereas DRE_{scl}^m indicates cooling effect (not shown). Over regions where aerosols are predominately non-absorbing, DRE_{all}^m indicates stronger cooling effect than DRE_{scl}^m . In this case, aerosols increase the reflection of the cloudy column.

[39] The presence of clouds reduces the surface cooling by about 30% (to -7.2 Wm^{-2} , Figures 8c and 9c). However, clouds have very little effect on atmospheric aerosol absorption, the global mean absorption is only 0.1 Wm^{-2} different from its clear-sky counterpart (Figures 8b and 9b). This is because for aerosols above clouds, the presence of clouds increases the absorption, while for aerosols below clouds, the presence of clouds decreases the absorption.

[40] All-sky DREs calculated using MODIS/MATCH aerosols differ from those calculated using GOCART aerosols by 38% (1.2 Wm^{-2}), 10% (0.3 Wm^{-2}), and 24% (1.5 Wm^{-2}) at the TOA, within the atmosphere, and at the surface under all-sky conditions (Table 3). Recall both DRE calculations use the same cloud properties. Comparing global distributions of DRE_{all}^m and DRE_{all}^g at the TOA for JJA 2004 (Figures 9a and 9d), we notice that DRE_{all}^g shows warming effect over the northern Pacific Ocean and over the Tibetan Plateau, while DRE_{all}^m indicates cooling effect over these regions. However,

Table 3. Annual mean all-sky direct aerosol radiative effect (Wm^{-2}) at the top-of-atmosphere, within the atmosphere, and at the surface derived using MODIS/MATCH aerosols (DRE_{all}^m) and GOCART aerosols (DRE_{all}^g) by explicitly accounting for clouds in the atmosphere over the globe, ocean, land, Northern Hemisphere (NH), and Southern Hemisphere (SH)¹

	Global		Ocean		Land		NH		SH	
	DRE_{all}^m	DRE_{all}^g	DRE_{all}^m	DRE_{all}^g	DRE_{all}^m	DRE_{all}^g	DRE_{all}^m	DRE_{all}^g	DRE_{all}^m	DRE_{all}^g
TOA	-3.08	-1.92	-2.74	-1.55	-3.98	-2.87	-3.94	-2.85	-2.23	-1.00
Atmos	3.25	2.91	1.91	1.95	6.76	5.42	4.11	4.01	2.41	1.83
Sfc	-6.33	-4.83	-4.65	-3.51	-10.74	-8.30	-8.05	-6.86	-4.64	-2.83

¹ Mean values are calculated from 60°N to 60°S.

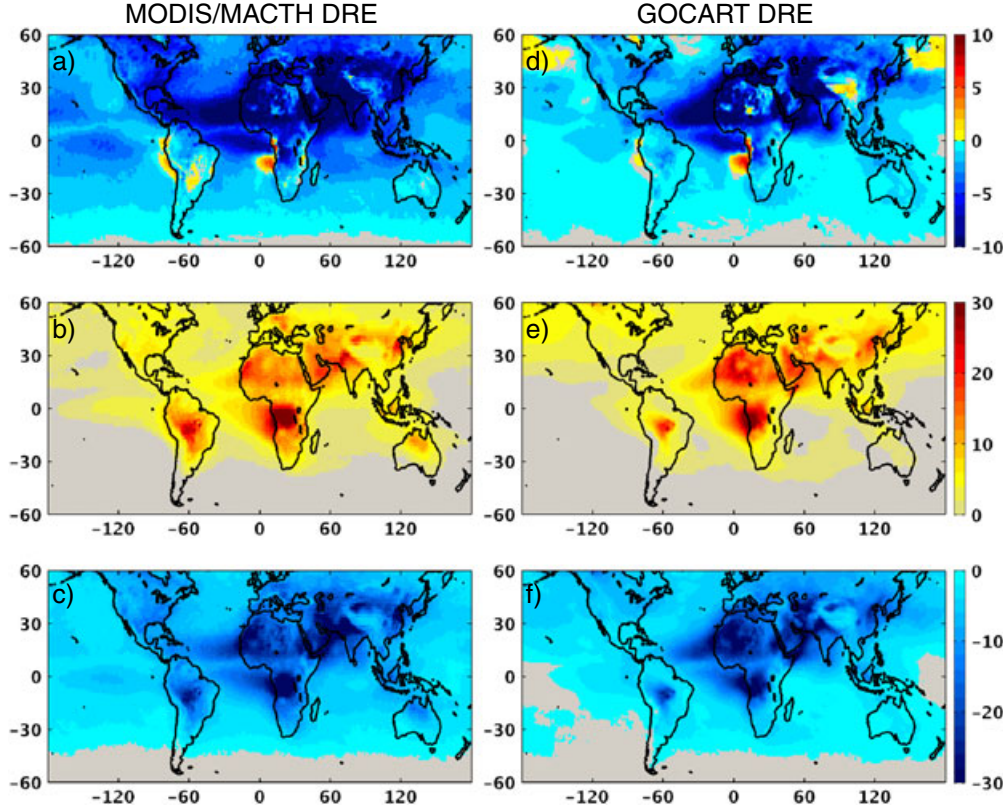


Figure 9. All-sky aerosol direct radiative effect (Wm^{-2}) for JJA 2004 at (a and d) the TOA (gray color indicates DRE is within $\pm 0.25 \text{ Wm}^{-2}$), (b and e) within the atmosphere (gray indicates atmospheric absorption is less than 1 Wm^{-2}), and (c and f) at the surface (gray indicates surface cooling is less than 1 Wm^{-2}). The left panels are from MODIS/MATCH aerosols, and the right panels are from GOCART aerosols.

over biomass burning regions of South America, the reverse is true. Over heavily polluted regions of eastern China, India, and North America, DRE_{all}^m predicts stronger cooling effect than DRE_{all}^g . These differences in DRE_{all}^m and DRE_{all}^g can partly be explained by $\Delta\Omega$ (Figure 6c). Under all-sky conditions, more absorbing aerosols will lead to less cooling effects if they are below the clouds but will lead to more warming effects if they are above the clouds. At the surface, DRF_{all}^m indicates stronger surface cooling than DRF_{all}^g except over northern Pacific, part of Europe, and northern Africa and off the west coast of northern Africa. Within the atmosphere, DRE_{all}^m indicates stronger atmospheric absorption than DRE_{all}^g over biomass burning regions of South America, southern Africa, and Indonesia. This is also true over eastern United States, India, and Eastern Europe.

3.3. Aerosol Direct Radiative Forcing

[41] Based upon the anthropogenic and natural aerosols prescribed by GOCART, we calculate the GOCART DRF and the partition ratio $k = DRF/DRE$ for every $1^\circ \times 1^\circ$ grid box every 3 h under clear-sky and all-sky conditions. This partition ratio is then applied to MODIS/MATCH DRE to derive the forcing components.

3.3.1. Clear-sky Aerosol Direct Radiative Forcing

[42] The annual mean clear-sky DRFs are listed in Table 4. Over ocean, the MODIS/MATCH DRF (DRF_{clr}^m) at the TOA is -1.4 Wm^{-2} , which is consistent with other observational-based estimates of $-1.1 \pm 0.37 \text{ Wm}^{-2}$ [Kaufman et al., 2005; Bellouin et al., 2005, 2008; Yu et al., 2006; Quaas et al., 2008; Matsui and Pielke, 2006; Christopher et al., 2006; Zhao et al., 2008]. The GOCART DRF (DRF_{clr}^g) at

Table 4. Annual mean clear-sky direct aerosol radiative forcing (Wm^{-2}) at the top-of-atmosphere, within the atmosphere, and at the surface derived from MODIS/MATCH aerosols (DRF_{clr}^m) and from GOCART (DRF_{clr}^g) over the globe, ocean, land, Northern Hemisphere (NH), and Southern Hemisphere (SH)¹

	Global		Ocean		Land		NH		SH	
	DRF_{clr}^m	DRF_{clr}^g	DRF_{clr}^m	DRF_{clr}^g	DRF_{clr}^m	DRF_{clr}^g	DRF_{clr}^m	DRF_{clr}^g	DRF_{clr}^m	DRF_{clr}^g
TOA	−1.55	−1.19	−1.39	−1.08	−1.98	−1.50	−1.86	−1.53	−1.25	−0.86
Atmos	2.57	2.07	1.74	1.49	4.75	3.59	2.81	2.49	2.34	1.65
Sfc	−4.12	−3.26	−3.13	−2.56	−6.72	−5.09	−4.67	−4.03	−3.59	−2.51

¹ Mean values are calculated from 60°N to 60°S.

the TOA is -1.1 Wm^{-2} , while the multimodel mean TOA DRF is -0.6 Wm^{-2} [Schulz *et al.*, 2006]. Note that the DRF in Schulz *et al.* [2006] is the difference between present day (2000) and pre-industrial (1750), whereas DRF in this study is the difference between total and natural aerosols. Over land, the TOA DRF_{clr}^m is about -2.0 Wm^{-2} , which is within the range (from -1.8 to -3.3 Wm^{-2}) of DRFs provided by a few studies [Yu *et al.*, 2006; Quaas *et al.*, 2008; Bellouin *et al.*, 2008]. The GOCART-based TOA DRF_{clr}^g is -1.5 Wm^{-2} , while the multimodel mean TOA DRF over land is about -1.1 Wm^{-2} [Schulz *et al.*, 2006]. Assuming the AERONET validation results (Figure 4) are applicable to the anthropogenic fractions, we expect that DRF_{clr}^g is more accurate than DRF_{clr}^m over land. At the surface, our global mean DRF_{clr}^m of -4.1 Wm^{-2} is on the low end of observational-based mean surface DRF [from -4.2 to 5.1 Wm^{-2} , Yu *et al.*, 2004; Bellouin *et al.*, 2005; Chung *et al.*, 2005; Matsui and Pielke, 2006], and the GOCART value is even lower (-3.3 Wm^{-2}). The surface cooling is stronger over land than over ocean, stronger over NH than over SH.

3.3.2. All-sky Aerosol Direct Radiative Forcing

[43] The annual mean all-sky DRFs are listed in Table 5. Our observational-based global mean DRF_{all}^m is -0.51 Wm^{-2} at the TOA, while previous observational-based estimates indicate that all-sky DRF ranges from -0.35 to -0.65 Wm^{-2} [Chung *et al.*, 2005; Bellouin *et al.*, 2008]. The GOCART model-based TOA all-sky DRF is -0.17 Wm^{-2} , while the multimodel mean is -0.22 Wm^{-2} [Schulz *et al.*, 2006]. To understand the difference between these two aerosol DRFs calculated from MODIS/MATCH and GOCART, we list the seasonal and annual mean TOA DRF_{all}^m and DRF_{all}^g over the globe and the 13 regions defined in Figure 10 in Table 6, and the corresponding surface values are listed in Table 7. We focus on the JJA distributions of DRF_{all}^m and DRF_{all}^g in detail below (Figure 11).

[44] In JJA, the TOA DRF_{all}^g shows significant warming over the northern Pacific and northern Atlantic Ocean, while DRF_{all}^m indicates cooling over these regions (Figures 11a and 11d). Furthermore, DRF_{all}^g shows more warming than DRF_{all}^m over Tibet and off the west coast of southern Africa. All these regions correspond to a positive $\Delta\omega$ difference (aerosols in GOCART are more absorbing, Figure 6c). However, DRF_{all}^g shows smaller warming effect than DRF_{all}^m over South America, where a negative $\Delta\omega$ is observed (Figure 6c). For regions where substantial cooling are observed, DRF_{all}^m produces stronger cooling than DRF_{all}^g . These regions include the east coast of the United States, the east coast of China, India, and over Indonesia, where τ_m is greater than τ_g (Figure 3c). Overall, the global mean TOA DRF_{all}^m is -0.52 Wm^{-2} , while DRF_{all}^g is -0.16 Wm^{-2} for this season. At the surface, DRF_{all}^m produces stronger cooling than DRF_{all}^g almost everywhere (Figures 11c and 11f), except over northern Pacific Ocean and off the west coast of Africa possibly due to stronger absorptions predicted by GOCART (Figure 6c). Within the atmosphere, DRF_{all}^g shows more atmospheric absorption than DRF_{all}^m over northern Pacific and northern Atlantic but shows less atmospheric absorption over eastern United States, South America, Eastern Europe, India, and Indonesia (Figures 11b and 11e).

[45] For every season, more regions exhibit warming effects in TOA DRF_{all}^g than in DRF_{all}^m . Additionally, over regions that are heavily polluted, TOA DRF_{all}^g shows smaller cooling effect than DRF_{all}^m . Therefore, the combined stronger warming and weaker cooling effects result in smaller cooling effect in the seasonal and annual mean TOA DRF_{all}^g than in DRF_{all}^m (by a factor of 2 to 6). Note that we derive DRF_{all}^m and DRF_{all}^g using the same cloud properties and surface albedo; thus, the differences in TOA DRF are all due to the differences in aerosol properties. Comparing the clear-sky and all-sky MODIS/MATCH DRFs with GOCART DRFs, although the presence of clouds reduces

Table 5. Annual mean all-sky direct aerosol radiative forcing (Wm^{-2}) at the top-of-atmosphere, within the atmosphere, and at the surface derived from MODIS/MATCH aerosols (DRF_{all}^m) and from GOCART aerosols (DRF_{all}^g) by explicitly accounting for clouds in the atmosphere over the globe, ocean, land, Northern Hemisphere (NH), and Southern Hemisphere (SH)¹

	Global		Ocean		Land		NH		SH	
	DRF_{all}^m	DRF_{all}^g	DRF_{all}^m	DRF_{all}^g	DRF_{all}^m	DRF_{all}^g	DRF_{all}^m	DRF_{all}^g	DRF_{all}^m	DRF_{all}^g
TOA	−0.51	−0.17	−0.49	−0.15	−0.57	−0.23	−0.67	−0.29	−0.35	−0.06
Atmos	2.51	2.02	1.78	1.53	4.45	3.30	2.70	2.36	2.34	1.68
Sfc	−3.02	−2.19	−2.27	−1.68	−5.02	−3.53	−3.37	−2.65	−2.69	−1.74

¹ Mean values are calculated from 60°N to 60°S.

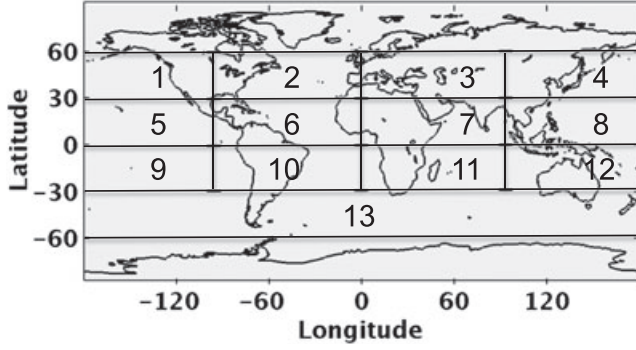


Figure 10. Locations of the 13 regions listed in Tables 6 and 7.

the magnitude of both, the differences between them ($DRF_{clr}^g - DRF_{clr}^m$ and $DRF_{all}^g - DRF_{all}^m$) remain almost unchanged. This is not surprising because under all-sky conditions the DRF is more sensitive to aerosol single-scattering albedo and aerosol vertical distribution than under clear-sky conditions [Loeb and Su, 2010]. We emphasize that the difference between DRF_{all}^m and DRF_{all}^g should not be used

to represent the uncertainty in all-sky DRF, as they are not entirely independent (both use the same clouds and both apply same mapping of all-sky DRE to DRF).

4. Summary

[46] We combine 3-hourly cloud properties from CERES SYN product with two aerosol data sets to calculate the clear-sky and all-sky aerosol DREs. The first aerosol data set is based upon MODIS aerosol optical depth retrieval and MATCH aerosol assimilation model (which assimilates MODIS aerosol optical depth); thus, this data set is largely constrained by MODIS aerosol optical depth. However, MATCH does not separate anthropogenic from natural aerosols, and we cannot calculate DRF from MODIS/MATCH alone. The other aerosol data set is based upon the GOCART model. The GOCART model predicts the anthropogenic and natural components of aerosols, and we therefore can calculate the aerosol DRF using GOCART. By assuming that the anthropogenic fractions from GOCART are correct, we thus apply the ratio of DRF to DRE based upon GOCART aerosol classifications to DRE calculated using MODIS/MATCH aerosols to partition it into DRF.

Table 6. Seasonal and annual mean all-sky direct aerosol radiative forcing (Wm^{-2}) at the top-of-atmosphere derived from the MODIS/MATCH aerosols (DRF_{all}^m) and GOCART aerosols (DRF_{all}^g) over regions from $60^\circ\text{N} \sim 60^\circ\text{S}$ and the 13 regions defined in Figure 10.

	DJF		MAM		JJA		SON		ANN	
	DRF_{all}^m	DRF_{all}^g	DRF_{all}^m	DRF_{all}^g	DRF_{all}^m	DRF_{all}^g	DRF_{all}^m	DRF_{all}^g	DRF_{all}^m	DRF_{all}^g
60–60	−0.47	−0.24	−0.44	−0.18	−0.52	−0.16	−0.60	−0.10	−0.51	−0.17
1	−0.14	0.01	−0.34	0.21	−0.78	0.43	−0.34	0.02	−0.40	0.17
2	−0.24	−0.07	−0.68	−0.22	−1.36	−0.41	−0.59	−0.26	−0.72	−0.24
3	−0.02	−0.06	−0.55	−0.69	−1.26	−1.10	−0.57	−0.58	−0.60	−0.61
4	−0.17	−0.05	−0.55	−0.12	−1.26	−0.01	−0.68	−0.30	−0.67	−0.12
5	−0.31	−0.14	−0.44	−0.19	−0.36	−0.15	−0.41	−0.22	−0.38	−0.17
6	−0.78	−0.61	−0.54	−0.38	−0.60	−0.42	−0.60	−0.38	−0.63	−0.45
7	−1.20	−0.83	−0.44	−0.14	−0.35	−0.03	−0.89	−0.35	−0.72	−0.34
8	−1.10	−0.53	−1.40	−0.37	−0.99	−0.34	−1.38	−0.69	−1.22	−0.48
9	−0.25	−0.10	−0.20	−0.09	−0.09	−0.02	−0.30	−0.06	−0.21	−0.07
10	−0.77	−0.55	−0.46	−0.28	−0.34	−0.37	−0.10	0.26	−0.42	−0.24
11	−0.77	−0.42	−0.41	−0.13	−0.37	−0.06	−0.51	0.07	−0.52	−0.13
12	−0.60	−0.21	−0.42	−0.16	−0.45	−0.20	−1.46	−0.55	−0.73	−0.28
13	−0.12	0.04	−0.09	−0.04	−0.07	0.05	−0.34	0.47	−0.15	0.13

Table 7. Seasonal and annual mean all-sky direct aerosol radiative forcing (Wm^{-2}) at the surface derived from MODIS/MATCH aerosols (DRF_{all}^m) and GOCART aerosols (DRF_{all}^g) over regions from $60^\circ\text{N} \sim 60^\circ\text{S}$ and the 13 regions defined in Figure 10.

	DJF		MAM		JJA		SON		ANN	
	DRF_{all}^m	DRF_{all}^g	DRF_{all}^m	DRF_{all}^g	DRF_{all}^m	DRF_{all}^g	DRF_{all}^m	DRF_{all}^g	DRF_{all}^m	DRF_{all}^g
60–60	−2.55	−1.79	−2.63	−1.93	−3.34	−2.51	−3.57	−2.53	−3.02	−2.19
1	−0.67	−0.61	−2.28	−2.77	−3.33	−2.85	−1.43	−1.08	−1.93	−1.83
2	−0.88	−0.65	−2.55	−2.70	−4.07	−3.08	−1.72	−1.28	−2.30	−1.93
3	−1.07	−0.92	−3.04	−3.55	−5.47	−4.74	−2.43	−2.07	−3.00	−2.82
4	−1.80	−1.55	−3.70	−4.75	−5.20	−5.13	−3.00	−2.57	−3.43	−3.50
5	−1.73	−0.78	−2.92	−1.81	−1.94	−1.13	−1.82	−1.02	−2.10	−1.19
6	−4.62	−3.56	−3.52	−2.26	−3.33	−2.46	−3.06	−2.06	−3.63	−2.59
7	−7.19	−6.19	−4.90	−3.00	−4.95	−4.21	−4.81	−3.16	−5.46	−4.14
8	−4.26	−2.49	−6.20	−4.81	−3.64	−2.82	−4.27	−2.82	−4.59	−3.24
9	−1.17	−0.52	−0.90	−0.33	−1.20	−0.52	−2.15	−1.35	−1.36	−0.68
10	−4.37	−2.83	−2.88	−1.21	−5.80	−3.90	−8.29	−5.56	−5.33	−3.38
11	−3.98	−2.79	−3.48	−1.43	−7.63	−5.33	−7.49	−4.42	−5.64	−3.49
12	−2.03	−1.08	−1.69	−0.72	−2.75	−1.16	−6.00	−3.94	−3.12	−1.72
13	−0.98	−0.64	−0.46	−0.30	−0.54	−0.49	−1.87	−1.95	−0.96	−0.84

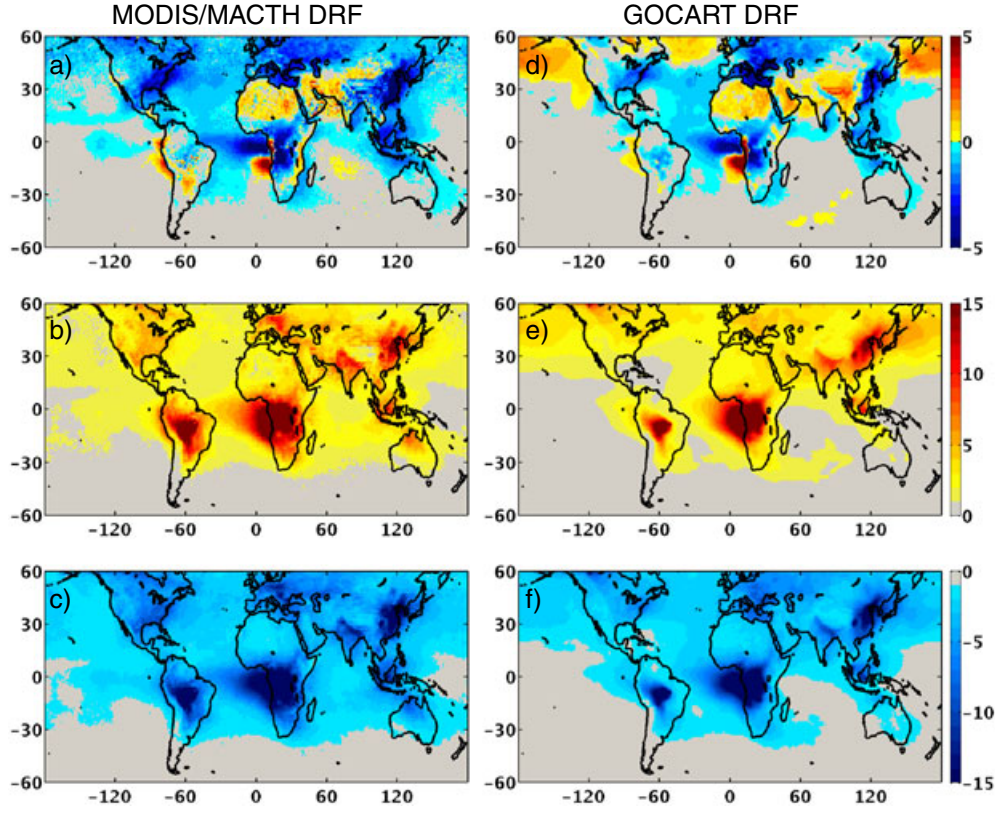


Figure 11. All-sky aerosol direct radiative forcing (Wm^{-2}) for JJA 2004 (a and d) at the TOA (gray color indicates forcing is within $\pm 0.25 \text{ Wm}^{-2}$), (b and e) within the atmosphere (gray indicates atmospheric absorption is less than 1 Wm^{-2}), and (c and f) at the surface (gray indicates surface cooling is less than 1 Wm^{-2}). The left panels are from MODIS/MATCH aerosols, and the right panels are from GOCART aerosols.

[47] Under clear-sky conditions, the global mean MODIS/MATCH DRFs are -1.55 , 2.57 , and -4.12 Wm^{-2} at the TOA, within the atmosphere, and at the surface. The corresponding GOCART DRFs are -1.19 , 2.07 , and -3.26 Wm^{-2} . The TOA DRF from MODIS/MATCH aerosols is within the range of published observational-based estimates, although the surface DRF is slightly smaller than published observational-based estimates. Our GOCART model-based TOA DRF indicates stronger cooling effects than published model-based DRF estimates.

[48] The all-sky DRFs based upon MODIS/MATCH aerosols are -0.51 Wm^{-2} at the TOA, 2.51 Wm^{-2} within the atmosphere, and -3.02 Wm^{-2} at the surface. The GOCART model-based DRFs are -0.17 Wm^{-2} at the TOA, 2.02 Wm^{-2} within the atmosphere, and -2.19 Wm^{-2} at the surface. The differences between these two DRFs are solely due to the differences in aerosol properties, since they are both derived using the same cloud properties and surface albedos and the same assumption about natural and anthropogenic contributions to the radiative effects of aerosols. We attribute the differences between MODIS/MATCH DRF and GOCART DRF to the smaller aerosol optical depths in the GOCART model than in the MODIS/MATCH; also, the aerosols in the GOCART model are more absorbing and possibly placed at a higher altitude than in MODIS/MATCH.

[49] Comparing the clear-sky and all-sky MODIS/MATCH DRFs with GOCART DRFs, we notice that the presence of

clouds greatly deteriorates the agreement between them at the TOA. Under clear-sky conditions, the relative difference $(1 - \text{DRF}_{\text{clr}}^g / \text{DRF}_{\text{clr}}^m)$ is 23%, while under all-sky conditions, the relative difference $(1 - \text{DRF}_{\text{all}}^g / \text{DRF}_{\text{all}}^m)$ increases to 67%. This highlights the complexity of determining the all-sky TOA DRF since the presence of clouds amplifies the sensitivities of DRF to aerosol single-scattering albedo and aerosol vertical distribution [Loeb and Su, 2010].

[50] Note the all-sky DRF computations discussed here explicitly consider clouds in the atmosphere at 3 h temporal resolution, unlike most published results which simply scale the clear-sky DRF by clear-sky fraction to approximate the all-sky DRF. Our comparison indicates that the scaled DRF tends to underestimate the TOA aerosol cooling effect if non-absorbing aerosols dominate and underestimates the TOA warming effect if absorbing aerosols dominate. Regionally, all-sky DRF differs from the scaled DRF by up to 200% at the TOA.

[51] Large difference between measurement-based and model-based all-sky DRF demonstrates the need for improved aerosol characterization from satellite and ground measurements. Aerosol optical depths simulated by models are systematically smaller than those retrieved from satellite measurements; thus, reducing the discrepancy in aerosol optical depth is the first step to narrow the difference in aerosol DRE and DRF. The large sensitivity of DRF to single-scattering albedo also emphasizes the need for

accurate global measurements of absorption by aerosol type. AERONET provides critical single-scattering albedo retrieval, but its spatial and temporal coverage prevent the establishment of a global aerosol absorption data set. New measurement techniques and retrieval algorithms are necessary as well to reduce the single-scattering albedo uncertainty under relatively small optical depth. Furthermore, under all-sky conditions, the vertical distribution of absorbing aerosols is also critical in determining all-sky DRF. Vertical profiles of absorbing aerosols from CALIPSO measurements provide an opportunity to constrain the aerosol vertical distribution among models. We expect the constrained aerosol vertical distribution to reduce the discrepancy of DRF from different models.

[52] **Acknowledgments.** This work was funded by NASA's Earth Science Enterprise. We thank Thomas Diehl and Qian Tan from NASA GSFC for providing GOCART simulations.

References

- Alexander, D., P. Crozier, and J. Anderson (2008), Brown carbon spheres in East Asian outflow and their optical properties, *Science*, **321**, 833–836.
- Anderson, T. L., Y. Wu, D. A. Chu, B. Schmid, J. Redemann, and O. Dubovik (2005), Testing the MODIS satellite retrieval of aerosol fine-mode fraction, *J. Geophys. Res.*, **110**, D18204, doi:10.1029/2005JD005978.
- Bellouin, N., O. Boucher, D. Tanre, and O. Dubovik (2003), Aerosol absorption over the clear-sky oceans deduced from POLDER-1 and AERONET observations, *Geophys. Res. Lett.*, **30**(14), 1748, doi:10.1029/2003GL017121.
- Bellouin, N., O. Boucher, J. Haywood, and M. S. Reddy (2005), Global estimate of aerosol direct radiative forcing from satellite measurements, *Nature*, **438**(22), 1138–1141.
- Bellouin, N., A. Jones, J. Haywood, and S. A. Christopher (2008), Updated estimate of aerosol direct radiative forcing from satellite observations and comparison against the Hadley centre climate model, *J. Geophys. Res.*, **113**(D10205), doi:10.1029/2007JD009385.
- Cattrell, C., K. L. Carder, and H. R. Gordon (2003), Columnar aerosol single-scattering albedo and phase function retrieved from sky radiance over the ocean: Measurements of Saharan dust, *J. Geophys. Res.*, **108**(D9), 4287, doi:10.1029/2002JD002497.
- Chakrabarty, R., H. Moosmüller, L.-W. Chen, K. Lewis, W. Arnott, C. Mazzoleni, M. Dubey, C. Wold, W. Hao, and S. Kreidenweis (2010), Brown carbon in tar balls from smoldering biomass combustion, *Atmos. Chem. Phys.*, **10**, 6363–6370, doi:10.5194/acp-10-6363-2010.
- Chand, D., R. Wood, T. L. Anderson, S. K. Satheesh, and R. J. Charlson (2009), Satellite-derived direct radiative effect of aerosols dependent on cloud cover, *Nature Geosci.*, **2**, 181–184.
- Charlock, T., and W. Sellers (1980), Aerosol effects on climate: Calculations with time-dependent and steady-state radiative-convective models, *J. Atmos. Sci.*, **37**, 1327–1341.
- Charlson, R., S. Schwartz, J. Hales, R. Cess, J. Coakley, J. Hansen, and D. Hofman (1992), Climate forcing by anthropogenic aerosols, *Science*, **255**, 423–430.
- Chin, M., P. Ginoux, S. Kinne, O. Torres, B. Holben, B. Duncan, R. Martin, J. Logan, A. Higurashi, and T. Nakajima (2002), Tropospheric aerosol optical thickness from the GOCART model and comparisons with satellite and sunphotometer measurements, *J. Atmos. Sci.*, **59**, 461–483.
- Chin, M., D. A. Chu, R. Levy, L. A. Remer, Y. J. Kaufman, B. N. Holben, T. Eck, and P. Ginoux (2004), Aerosol distribution in the Northern Hemisphere during ACE-Asia: Results from global model, satellite observations, and sunphotometer measurements, *J. Geophys. Res.*, **109**(D23S90), doi:10.1029/2004JD004829.
- Chin, M., T. Diehl, P. Ginoux, and W. Malm (2007), Intercontinental transport of pollution and dust aerosols: Implications for regional air quality, *Atmos. Chem. Phys.*, **7**, 5501–5517.
- Chin, M., T. Diehl, O. Dubovik, T. Eck, B. Holben, A. Sinyuk, and D. Streets (2009), Light absorption by pollution, dust, and biomass burning aerosols: A global model study and evaluation with AERONET measurements, *Ann. Geophys.*, **27**, 3439–3464.
- Christopher, S. A., J. Zhang, Y. J. Kaufman, and L. A. Remer (2006), Satellite-based assessment of top of atmosphere anthropogenic aerosol radiative forcing over cloud-free oceans, *Geophys. Res. Lett.*, **33**(L15816), doi:10.1029/2005GL025535.
- Chung, C. E., V. Ramanathan, D. Kim, and I. A. Podgorny (2005), Global anthropogenic aerosol direct forcing derived from satellite and ground-based observations, *J. Geophys. Res.*, **110**(D24207), doi:10.1029/2005JD006356.
- Chylek, P., and J. Coakley (1974), Aerosols and climate, *Science*, **183**, 75–77.
- Collins, W. D., P. J. Rasch, B. E. Eaton, B. V. Khattatov, J.-F. Lamarque, and C. S. Zender (2001), Simulating aerosols using a chemical transport model with assimilation of satellite aerosol retrievals: Methodology for INDOEX, *J. Geophys. Res.*, **106**, 7313–7336.
- Doelling, D. R., N. G. Loeb, D. F. Keyes, M. L. Nordeen, D. Morstad, B. A. Wielicki, D. F. Young, and M. Sun (2013), Geostationary enhanced temporal interpolation for CERES flux products, *J. Atmos. Oceanic Technol.* (under revision).
- Dubovik, O., B. Holben, T. Eck, A. Smirnov, Y. Kaufman, M. King, D. Tanre, and I. Slutsker (2002), Variability of absorption and optical properties of key aerosol types observed in worldwide locations, *J. Atmos. Sci.*, **59**, 590–608.
- Forster, P., et al. (2007), Changes in atmospheric constituents and in radiative forcing, in *Climate Change 2007: The Physical Science Basis. Contribution of working group I to the Fourth Assessment Report of the IPCC*, edited by S. Solomon, D. Qin, M. Manning, Z. Chen, M. Marquis, K. B. Averyt, M. Tignor, and H. L. Miller, Cambridge University Press, Cambridge, United Kingdom and New York, NY, USA.
- Fu, Q., and K.-N. Liou (1992), On the correlated-k distribution method for radiative transfer in nonhomogenous atmospheres, *J. Atmos. Sci.*, **49**, 2139–2156.
- Fu, Q., and K.-N. Liou (1993), Parameterization of the radiative properties of cirrus clouds, *J. Atmos. Sci.*, **50**, 2008–2025.
- Ginoux, P., M. Chin, I. Tegen, J. Prospero, B. Holben, O. Dubovik, and S.-J. Lin (2001), Sources and global distributions of dust aerosols simulated with the GOCART model, *J. Geophys. Res.*, **106**, 20,255–20,273.
- Ginoux, P., J. Prospero, O. Torres, and M. Chin (2004), Long-term simulation of dust distribution with the GOCART model: Correlation with the North Atlantic Oscillation, *Environ. Model. Software*, **19**, 113–128.
- Haywood, J., and K. Shine (1995), The effect of anthropogenic sulfate and soot on the clear sky planetary radiation budget, *Geophys. Res. Lett.*, **22**(5), 603–606.
- Hess, M., P. Koepke, and I. Schult (1998), Optical properties of aerosols and clouds: The software package OPAC, *Bull. Am. Meteor. Soc.*, **79**(5), 831–844.
- Hoffer, A., A. Gelencsér, P. Guyon, G. Kiss, O. Schmid, G. Frank, P. Artaxo, and M. Andreae (2006), Optical properties of humic-like substances (HULIS) in biomass-burning aerosols, *Atmos. Chem. Phys.*, **6**, 3563–3570.
- Jin, Z., T. P. Charlock, W. L. Smith Jr., and K. Rutledge (2004), A parameterization of ocean surface albedo, *Geophys. Res. Lett.*, **31**(22), doi:10.1029/2004GL021180.
- Kanakidou, M., J. H. Seinfeld, S. N. Pandis, I. Barnes, F. J. Dentener, M. C. Facchini, R. Van Dingenen, B. Ervens, A. Nenes, C. J. Nielsen, E. Swietlicki, J. P. Putaud, Y. Balkanski, S. Fuzzi, J. Horth, G. K. Moortgat, R. Winterhalter, C. E. L. Myhre, K. Tsigaridis, E. Vignati, E. G. Stephanou, and J. Wilson (2005), Organic aerosol and global climate modelling: A review, *Atmospheric Chem. Phys.*, **5**(4), 1053–1123.
- Kaufman, J. Y., D. Tanre, O. Dubovik, A. Karnieli, and L. A. Remer (2001), Absorption of sunlight by dust as inferred from satellite and ground based remote sensing, *Geophys. Res. Lett.*, **28**, 1479–1483.
- Kaufman, Y. J., O. Boucher, D. Tanre, M. Chin, L. A. Remer, and T. Takemura (2005), Aerosol anthropogenic component estimated from satellite data, *Geophys. Res. Lett.*, **32**(L17804), doi:10.1029/2005GL023125.
- Kinne, S., U. Lohmann, J. Feichter, M. Schulz, C. Timmreck, S. Ghan, R. Easter, M. Chin, P. Ginoux, T. Takemura, I. Tegen, D. Koch, M. Herzog, J. Penner, G. Pitari, B. Holben, T. Eck, A. Smirnov, O. Dubovik, I. Slutsker, D. Tanre, O. Torres, M. Mishchenko, I. Geogdzhayev, D. Chu, and Y. Kaufman (2003), Monthly averages of aerosol properties: A global comparison among models, satellite data, and AERONET ground data, *J. Geophys. Res.*, **108**(D20), 4634, doi:10.1029/2001JD001253.
- Kirchstetter, T., T. Novakov, and P. Hobbs (2004), Evidence that spectral dependence of light absorption by aerosols is affected by organic carbon, *J. Geophys. Res.*, **109**, D21208, doi:10.1029/2004JD004999.
- Koffi, B., et al. (2012), Application of the CALIOP layer product to evaluate the vertical distribution of aerosols estimated by global models: AeroCom phase I results, *J. Geophys. Res.*, **117**(D10201), doi:10.1029/2011JD016858.
- Levin, E. J. T., et al. (2010), Biomass burning smoke aerosol properties measured during Fire Laboratory at Missoula Experiments (FLAME), *J. Geophys. Res.*, **115**, D18210, doi:10.1029/2009JD013601.
- Liao, H., and J. Seinfeld (1998), Effect of clouds on direct aerosol radiative forcing of climate, *J. Geophys. Res.*, **103**(D4), 3781–3788.

- Loeb, N. G., and N. Manalo-Smith (2005), Top-of-atmosphere direct radiative effect of aerosols over global oceans from merged CERES and MODIS observations, *J. Climate*, **18**, 3506–3526.
- Loeb, N. G., and W. Su (2010), Direct aerosol radiative forcing uncertainty based on a radiative perturbation analysis, *J. Climate*, **23**, 5288–5293, doi:10.1175/2010JCLI3543.1.
- Matsui, T., and R. S. Pielke (2006), Measurement-based estimation of the spatial gradient of aerosol radiative forcing, *Geophys. Res. Lett.*, **33** (L11813), doi:10.1029/2006GL025974.
- Minnis, P., W. L. J. Smith, D. P. Garber, J. K. Ayers, and D. R. Doelling (1995), Cloud properties derived from GOES-7 for the spring 1994 ARM intensive observing period using version 1.0.0 of the ARM satellite data analysis program, Tech. rep., NASA RP 1366.
- Minnis, P., L. Nguyen, D. R. Doelling, D. F. Young, and W. Miller (2002), Rapid calibration of operational and research meteorological satellite imagers. Part I: Evaluation of research satellite visible channels as references, *J. Atmos. Oceanic Technol.*, **19**, 1233–1249.
- Minnis, P., C. R. Trepte, S. Sun-Mack, Y. Chen, D. R. Doelling, D. F. Young, D. A. Spangenberg, W. F. Miller, B. A. Wielicki, R. R. Brown, S. C. Gibson, and E. B. Geier (2008), Cloud detection in nonpolar regions for CERES using TRMM VIRS and TERRA and AQUA MODIS data, *IEEE Trans. Geosci. Remote Sens.*, **46**(11), 3857–3884.
- Minnis, P., D. F. Sun-Mack, S. Young, P. W. Heck, D. P. Garber, Y. Chen, D. A. Spangenberg, R. F. Arduini, Q. Z. Trepte, W. L. J. Smith, J. K. Ayers, S. C. Gibson, W. F. Miller, V. Chakrapani, Y. Takano, K. Liou, and Y. Xie (2011), CERES Edition-2 cloud property retrievals using TRMM VIRS and TERRA and AQUA MODIS data, Part I: Algorithms, *IEEE Trans. Geosci. Remote Sens.*, **49**(11), doi:10.1109/TGRS.2011.2144601.
- Myhre, G. (2009), Consistency between satellite-derived and modeled estimates of the direct aerosol effect, *Science*, **325**, 187–190.
- Podgorny, I. A., and V. Ramanathan (2001), A modeling study of the direct effect of aerosols over the tropical Indian Ocean, *J. Geophys. Res.*, **106**, 24,097–24,105.
- Quaas, J., O. Boucher, N. Bellouin, and S. Kinne (2008), Satellite-based estimate of the direct and indirect aerosol climate forcing, *J. Geophys. Res.*, **113**(D05204), doi:10.1029/2007JD008962.
- Remer, L. A., Y. Kaufman, D. Tanre, S. Mattoo, D. A. Chu, J. V. Martins, and coauthors (2005), The MODIS aerosol algorithm, products, and validation, *J. Atmos. Sci.*, **62**, 947–973.
- Rose, F. G., and T. P. Charlock (2002), New Fu-Liou code tested with ARM Raman Lidar and CERES in pre-CALIPSO Sensitivity Study, in Extended Abstract for 11th Conference on Atmospheric Radiation, Ogden, UT, *Amer. Meteor. Soc.*, P4.8.
- Rutan, D., F. Rose, M. Roman, N. Manalo-Smith, C. B. Schaaf, and T. Charlock (2009), Development and assessment of broadband surface albedo from clouds and the Earth's Radiant Energy System Clouds and Radiation Swath data product, *J. Geophys. Res.*, **114**(D08125), doi:10.1029/2008JD010669.
- Schnaiter, M., M. Gimmmler, I. Llamas, C. Linke, C. Jäger, and H. Mutschke (2006), Strong spectral dependence of light absorption by organic carbon particles formed by propane combustion, *Atmos. Chem. Phys.*, **6**, 2981–2990.
- Schulz, M., et al. (2006), Radiative forcing by aerosols as derived from the AeroCom present-day and pre-industrial simulations, *Atmos. Chem. Phys.*, **6**, 5225–5246.
- Sinyuk, A., O. Torres, and O. Dubovik (2003), Combined use of satellite and surface observations to infer the imaginary part of refractive index of Saharan dust, *Geophys. Res. Lett.*, **30**, doi:10.1029/2002GL016189.
- Stubenrauch, C. J., S. Kinne, and the GEWEX cloud assessment team (2009), Assessment of global cloud climatologies, *GEWEX News*, **19** (1), 6–7.
- Yang, S.-K., S. Zhou, and A. L. Miller (1999), SMOBA: A 3-dimensional daily ozone analysis using SBUV/2 and TOVS measurement, <http://www.cpc.ncep.noaa.gov/products/stratosphere/SMOBA/>.
- Yu, H., R. E. Dickinson, M. Chin, J. Y. Kaufman, M. Zhou, L. Zhou, Y. Tian, O. Dubovik, and B. N. Holben (2004), Direct radiative effect of aerosols as determined from a combination of MODIS retrievals and GOCART simulations, *J. Geophys. Res.*, **109**, doi:10.1029/2003JD003914.
- Yu, H., et al. (2006), A review of measurement-based assessments of the aerosol direct radiative effect and forcing, *Atmos. Chem. Phys.*, **6**, 613–666.
- Yu, H., P. K. Quinn, G. Feingold, L. A. Remer, R. A. Kahn, M. Chin, and S. Schwartz (2009), Remote sensing and in situ measurements of aerosol properties, burdens, and radiative forcing, in *Atmospheric Aerosol Properties and Climate Impacts*, edited by M. Chin, R. A. Kahn, and S. E. Schwartz, A Report by the U.S. Climate Change Science Program and the Subcommittee on Global Change Research, National Aeronautics and Space Administration, Washington, D. C., USA.
- Yu, H., M. Chin, D. M. Winker, A. H. Omar, Z. Liu, C. Kittaka, and T. Diehl (2010), Global view of aerosol vertical distributions from CALIPSO lidar measurements and GOCART simulations: Regional and seasonal variations, *J. Geophys. Res.*, **115**, doi:10.1029/2009JD013364.
- Zhao, T. X.-P., H. Yu, I. Laszlo, M. Chin, and W. C. Conant (2008), Derivation of component aerosol direct radiative forcing at the top of atmosphere for clear-sky oceans, *J. Quant. Spect. Rad. Trans.*, **109**, 1162–1186.